Giant tunneling magnetoresistance and electroresistance in α-In$_2$Se$_3$-based van der Waals multiferroic tunnel junctions

Zhi Yan [ORCID],[1] Zeyu Li,[2] Yulei Han [ORCID],[3,*] Zhenhua Qiao,[2,†] and Xiaohong Xu[1,‡]

[1]*School of Chemistry and Materials Science of Shanxi Normal University & Key Laboratory of Magnetic Molecules and Magnetic Information Materials of Ministry of Education, Research Institute of Materials Science of Shanxi Normal University & Collaborative Innovation Center for Shanxi Advanced Permanent Magnetic Materials and Technology, Linfen 041004, China*
[2]*ICQD, Hefei National Laboratory for Physical Sciences at Microscale, CAS Key Laboratory of Strongly-Coupled Quantum Matter Physics, and Department of Physics, University of Science and Technology of China, Hefei, Anhui 230026, China*
[3]*Department of Physics, Fuzhou University, Fuzhou, Fujian 350108, China*

In the multiferroic tunnel junction (MFTJ) composed of ferromagnetic and ferroelectric materials, the tunneling electroresistance (TER) coexists with the tunneling magnetoresistance (TMR), making it an ideal platform for designing multifunctional electronic devices. Recently, the rapid development of van der Waals (vdW) materials opened up a new avenue of MFTJ due to their atomic thickness and significance in miniaturizing device sizes. Here by employing the nonequilibrium Green's function combined with density-functional theory, we systemically study the spin-dependent electronic transport properties of Fe$_3$GeTe$_2$ (FGT)/bilayer α-In$_2$Se$_3$ (BIS)/FGT vdW MFTJs. We find that the MFTJ can form multiple nonvolatile resistance states by altering the polarization orientation of the ferroelectric barrier BIS and the magnetization alignment of the two ferromagnetic FGT electrodes, with a maximum TMR (TER) ratio up to $1.1 \times 10^7\%$ (744%). The TER ratio can be further increased to 1868% by using left and right symmetrical copper electrodes. More interestingly, the perfect spin filtering effect can be realized in our MFTJs and the spin current can be controlled by the sign of bias voltages, suggesting a promising route for spin valves that can flexibly manipulate spin currents. Our results demonstrate that giant TMR, large TER, as well as a tunable spin filter can coexist in one system, and that the feasible tunability of such kind of vdW MFTJs is beneficial in designing next-generation logic and memory devices.

I. INTRODUCTION

Tunnel junctions, usually established by a sandwich structure consisting of metal/insulator/metal regime, are crucial in the magnetic recording process where the spin orientations manipulated during the rapid reading and writing procedures are utilized to store binary information [1,2]. By changing the tunnel junction materials, one can construct different types of devices, e.g., magnetic tunnel junctions (TJs) [3,4], ferroelectric TJs [5], and multiferroic TJs (MFTJs) [6,7]. Compared with magnetic TJs and ferroelectric TJs, the MFTJs exhibit multiple nonvolatile resistance states characterized by the coexisting tunnel magnetoresistance (TMR) and tunnel electroresistance (TER). The TMR and TER in MFTJs can be separately manipulated by applying external magnetic fields to alter the magnetic directions of electrodes or by applying electric fields to reverse the ferroelectric polarization direction of the barrier layer [8], demonstrating feasible tunability and multifunctional applications in MFTJs.

Generally, the MFTJs are constructed by coupling a ferroelectric barrier with magnetic electrodes [8,9]. Until now,

the perovskite oxide materials are usually utilized as ferroelectric barrier layers in MFTJs [10–13]. However, the performance of perovskite oxide-based MFTJs is affected by natural defects, interfacial contact resistance, and dangling bonds during the fabrication of devices, which hinders the realistic application of MFTJs. Fortunately, the abundant van der Waals (vdW) materials, harboring quasiplane structures without dangling bonds, open up a perfect approach to investigate magnetic/ferroelectric TJs [14–29] and MFTJs [30]. Compared with traditional bulk materials, the performance of vdW-based tunnel devices can be greatly improved mainly due to the controllable layer thickness and perfect interface of vdW materials.

Lots of ferromagnetic/ferroelectric vdW materials have been experimentally synthesized. For example, layered Fe$_3$GeTe$_2$ (FGT) displays metallic and ferromagnetic properties with the Curie temperature up to 220 K and strong perpendicular magnetic anisotropy [31,32], and the Curie temperature can be further increased beyond room temperature by ionic gate regulation [33]. Thus FGT is a suitable candidate for MFTJs as electrode material. For the family of vdW ferroelectric materials [34–38], α-In$_2$Se$_3$ demonstrates room-temperature ferroelectricity with both in-plane and out-of-plane polarization [34]. In bilayer In$_2$X$_3$ (X = S, Se, Te), the vdW antiferroelectric TJ has been proposed which exhibits huge TER and multiple nonvolatile resistance states due to the

*Corresponding author: han@fzu.edu.cn
†Corresponding author: qiao@ustc.edu.cn
‡Corresponding author: xuxh@sxnu.edu.cn

switchable electric polarization [39], implying that α-In$_2$Se$_3$ is appropriate for MFTJs as barrier layers. Therefore the rapid development of ferromagnetic/ferroelectric vdW materials provides an ideal platform to explore MFTJs at atomic scale by coupling them together. The vdW MFTJs are not only experimentally feasible since the advanced crystal technologies but also tunable in different ways, e.g., electric/magnetic field, stacking order, etc. Recently, the vdW MFTJ consisting of PtTe$_2$ electrodes and monolayer In$_2$Se$_3$ barrier layers with ferromagnetic Fe$_n$GeTe$_2$ (n = 3, 4, 5) multilayer has been proposed, in which the reported TMR (TER) ratio approaches about 89% (62%) [30].

In this work, we theoretically investigate the spin-dependent electronic transport properties of Fe$_3$GeTe$_2$/bilayer α-In$_2$Se$_3$/Fe$_3$GeTe$_2$ (FGT/BIS/FGT) vdW MFTJs. Due to the multiple polarization states of bilayer α-In$_2$Se$_3$, this type of device is highly tunable by external electric field. We find a giant TMR ratio up to 1.1×10^7% in the MFTJs by changing the magnetic orientation of FGT electrodes from parallel (P) to antiparallel (AP) arrangement and large TER ratio up to 744% by ferroelectric-antiferroelectric order transitions of bilayer In$_2$Se$_3$. Interestingly, we observe a perfect spin filtering effect in the MFTJs, and the spin current can be controlled by the sign of bias voltages when FGT electrodes are exhibiting AP order. We further investigate the influence of electrodes on the performance of the MFTJs, i.e., symmetric Cu-FGT/BIS/FGT-Cu and asymmetric Cu-FGT/BIS/FGT geometries. In both systems, a large TER ratio can be obtained whereas the spin filtering effect is preserved, e.g., the system with symmetric Cu electrodes exhibits 1868% TER. Our findings demonstrate the exotic electronic/spintronic states of vdW MFTJs and provide an appropriate platform for further experimental exploration of vdW MFTJs.

II. COMPUTATIONAL METHODS

The structural optimization, total energy, and band-structure calculations of all systems were performed by using the projected augmented-wave [40] method as implemented in the Vienna *ab initio* simulation package (VASP) [41]. The generalized gradient approximation of the Perdew-Burke-Ernzerhof type was used to treat the exchange-correlation interaction [42]. The kinetic energy cutoff was set to be 500 eV. A vacuum space of 20 Å was considered to avoid interaction between neighboring slabs. All atoms were fully relaxed until the energy (10^{-6} eV) and force (0.01 eV/Å) convergence criteria were reached. The DFT-D3 type of vdW force correction was included in our calculations [43]. The Γ-centered k-mesh points of $15 \times 15 \times 1$ were used for structural optimization and total-energy estimation.

The electronic transport properties were calculated by using density-functional theory coupled with the nonequilibrium Green's function [44] as implemented in the Nanodcal package [45]. The plane-wave cutoff energy was set to be 80 hartree. The double-ζ polarized atomic-orbital basis was used to expand all physical quantities [46]. In self-consistent calculation, the energy convergence criterion of Hamiltonian matrix was set to be 10^{-6} eV. More $100 \times 100 \times 1$ k-mesh points were set for calculating the spin-reversed current and transmission coefficients of all MFTJs.

In the linear-response regime, the spin-polarized current I_σ and conductance G_σ are defined by the Landauer-Büttiker formula [47,48]

$$I_\sigma = \frac{e}{h} \int T_\sigma(E)[f_L(E) - f_R(E)]dE, \qquad (1)$$

$$G_\sigma = \frac{e^2}{h}T_\sigma, \qquad (2)$$

where $\sigma = \uparrow, \downarrow$ denotes the index of spin, e is the electron charge, h is Planck's constant, $T_\sigma(E)$ is the spin-resolved transmission coefficient, and $f_{L(R)}(E)$ is the Fermi-Dirac distribution function of the left (right) electrode. The formula $I = I_\uparrow + I_\downarrow$ is used to calculate the total charge current I. The spin injection efficiency (η) can be defined as

$$\eta = \left| \frac{I_\uparrow - I_\downarrow}{I_\uparrow + I_\downarrow} \right|. \qquad (3)$$

The TMR ratio in equilibrium state (without bias voltage) is calculated by [49]

$$\text{TMR} = \frac{G_P - G_{AP}}{G_{AP}} = \frac{T_P - T_{AP}}{T_{AP}}, \qquad (4)$$

where T_P and T_{AP} are the total transmission coefficient of MFTJs in and AP magnetic states, respectively. Similarly, TER ratio is defined as [23,24,50]

$$\text{TER} = \frac{G_{\max} - G_{\min}}{G_{\min}} = \frac{T_{\max} - T_{\min}}{T_{\min}}, \qquad (5)$$

where $T_{\max}$ and $T_{\min}$ are the total transmission coefficient of MFTJs at the Fermi level which can be obtained by reversing the direction of the ferroelectric polarization of the barrier layer.

III. RESULTS AND DISCUSSION

A. The atomic model of MFTJs

The α-In$_2$Se$_3$ belongs to the $R3m$ space group and its layers are stacked along the z axis by vdW interaction [34,51]. The weak vdW interaction of α-In$_2$Se$_3$ layers means that few layers of α-In$_2$Se$_3$ can be exfoliated from its bulk, which has been experimentally realized [52,53]. Each α-In$_2$Se$_3$ monolayer is composed of five atomic layers with a Se-In-Se-In-Se sequence [34]. For each atomic layer, there are three inequivalent high-symmetry sites labeled as A/B/C [see Fig. 1(a)]. The ferroelectricity of monolayer α-In$_2$Se$_3$ mainly originates from the dipole interaction between the middle In-Se bond along the z direction. For BIS, as displayed in Fig. 1(a), there are three different dipole arrangements, i.e., (i) FE, (ii) tail-to-tail (marked as AFE-Tail), and (iii) head-to-head (marked as AFE-Head) states. We first investigate the stacking-dependent structural stability of the three states. By translating the top layer whereas fixing the bottom layer, we can obtain three different stacking orders, i.e., Se$_1$-A, Se$_1$-B, and Se$_1$-C, where Se$_1$ denotes the atom marked with a dotted circle in Fig. 1(a). The total-energy calculation shows that the Se$_1$-B geometry is stable for both FE and AFE-Tail states, whereas the Se$_1$-C structure is preferred for the AFE-Head state as shown in Fig. 1(b). Moreover, the reported transition barrier between these states is about 30–40 meV [39], which is comparable to the FE switching barrier of a typical three-dimensional (3D)
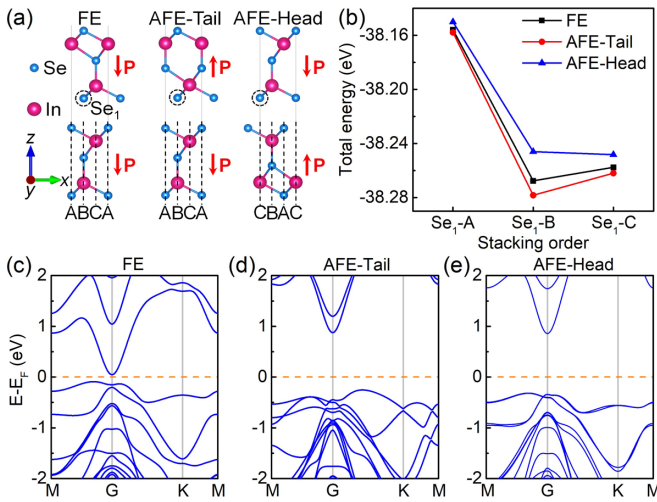
FIG. 1. (a) The crystal structures of BIS with three different ferroelectric polarizations (indicated by red arrows), i.e., FE, AFE-Tail, and AFE-Head states. (b) The total energy of BIS at three polarized states as a function of the various stacking orders. The band structures of BIS at FE (c), AFE-Tail (d), and AFE-Head (e) states. The Fermi level is set to zero.

perovskite oxide. Thus these states can be switched to each other by an external electric field. Hereinbelow, we choose the most stable stacking geometries as the structure of the three dipole states.

Figures 1(c)–1(e) display the band structures of BIS for different dipole states calculated by using the hybrid Heyd-Scuseria-Eenzerhof (HSE06) exchange-correlation functional. The three dipole structures exhibit an indirect gap, and the gap in the two AFE states is larger than that in the FE state, which is mainly due to the bands shift BIS caused by the depolarized electric field produced by out-of-plane ferroelectric polarization in the FE state [39,54]. Therefore the semiconducting characteristic of the three dipole structures indicates that BIS is suitable for the ferroelectric barrier layer in MFTJs.

After obtaining the optimized structure of the ferroelectric barrier layer, we can build the FGT/BIS/FGT vdW MFTJ. The in-plane lattice constants of FGT and α-In$_2$Se$_3$ are, respectively, 3.991 [31,55] and 4.025 Å [52,56], so the small lattice mismatch (0.85%) allows us to construct a heterojunction with a 1×1 unit cell. Like BIS, the favorable stacking configurations of the MFTJs can be determined by translating the bottom/top FGT electrodes. Due to the presence of inversion symmetry, the MFTJ forms six types of stacking orders, i.e., Te$_1$(A)-Te$_2$(A), Te$_1$(A)-Te$_2$(B), Te$_1$(A)-Te$_2$(C), Te$_1$(B)-Te$_2$(B), Te$_1$(B)-Te$_2$(C), and Te$_1$(C)-Te$_2$(C), where Te$_{1/2}$ represents a Te layer in the bottom/top FGT electrode and A/B/C denotes the high-symmetry sites of lattice [see Fig. 2(a)]. The total-energy evaluation for the above six different structures is summarized in Fig. 2(b). We can see that the Te$_1$(C)-Te$_2$(C) configuration is favorable for FE and AFE-Tail states, while Te$_1$(B)-Te$_2$(C) is preferred for the AFE-head state [see Fig. 2(a)]. After determining the stacking order of the FGT/BIS interfaces, we can construct the complete transport device of the FGT/BIS/FGT MFTJ by coupling BIS with two FGT electrodes, as displayed in Fig. 2(c). The central

scattering region contains a BIS ferroelectric barrier layer and trilayer FGT electrodes as buffer layers. The magnetization of FGT and the ferroelectric polarization of BIS are tunable, so multiple nonvolatile resistance states can be induced in the vdW MFTJs.

B. Significant TMR and TER effects in equilibrium state

As discussed above, the magnetic FGT electrodes have two states (P/AP) while the ferroelectric α-In$_2$Se$_3$ bilayer has three states (FE/AFE-Tail/AFE-Head), indicating that six combined states can be induced in the MFTJ. First we study the TMR and TER effects of the FGT/BIS/FGT vdW MFTJs in the equilibrium state. As summarized in Table I, the TMR ratio depends on the ferroelectric polarization of BIS, i.e., the TMR for FE, AFE-Tail, and AFE-Head states are 3.9×10^6, 1.12×10^7, and 7.6×10^6%, respectively. It is worth noting that the tiny value of $T_{\uparrow/\downarrow}$ is converged by our k-mesh test. Compared with a previous study [30], the TMR ratio in our vdW MFTJs is large enough to be implemented in spintronic devices such as magnetic sensors, hard disk read heads, and magnetoresistive random access memories.

Besides the TMR effect, the TER effect is also crucial to evaluate the performance of the FGT/BIS/FGT MFTJs. According to the total-energy calculation displayed in Fig. 1(b), we choose the ground state as the AFE-Tail to evaluate the TER ratio. As shown in Table I, the total transmission coefficient T_{tot} for the AFE-Tail state is the smallest among the three ferroelectric polarization states. When the polarization of BIS is switched to the FE state, the TER ratio in the P (AP) magnetic state is 182% (701%). When its polarization is switched to the AFE-Head state, the TER ratio becomes larger, i.e., 493% (744%) in the P (AP) state. Therefore the FGT/BIS/FGT vdW MFTJs harbor proper TER ratios and may have great application potential in nonvolatile memory devices. To further clarify the multiple nonvolatile resistance states in these MFTJs, we calculate the PDOS of the central scattering region in the (E, z) plane, where E represents the Fermi energy and z denotes vertical distance along the transport direction. Figure 3 displays the spin-resolved PDOS of the central scattering region for the three types of ferroelectric states. The low PDOS for the BIS region (around the position from 25 to 42 Å) indicates that BIS is sufficiently thick as an insulating barrier layer and the transmission is mainly determined by the magnetic electrodes. Clearly, a typical TMR effect can be reflected from the PDOS digram. Due to the three types of ferroelectric states that show similar PDOS patterns at $E = 0$, we choose the FE state to analyze the transmission of the MFTJs. Note that here we treat the spin-down PDOS of FGT at the P state as minority states. This is because FGT is located at approximately 7.5, 17.5, 55, and 65 Å at the Fermi level, where there is almost no DOS as highlighted by the black rectangles in Fig. 3(a). For the AP state, electrons with spin-up (spin-down) flow from the left FGT to the BIS ferroelectric barrier layer with majority (minority) states at the Fermi level flow out of the BIS and then pass through the right FGT with minority (majority) states. The correspondence between the FGT layers on both sides of the BIS with an inverted DOS number undoubtedly obstructs electron transport, indicating the presence of
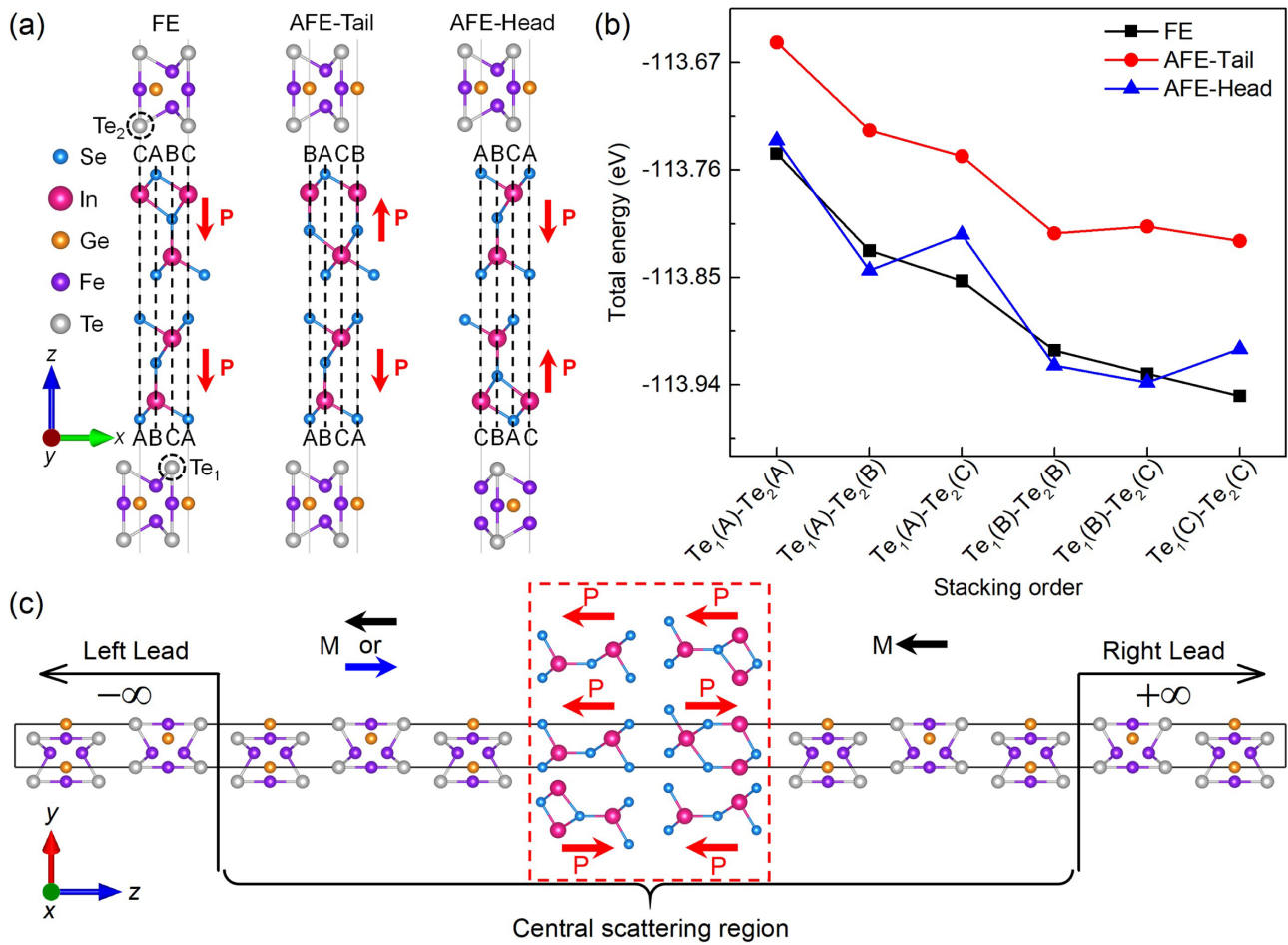
FIG. 2. (a) Crystal structures of FGT/BIS/FGT sandwich heterojunction. (b) The total energy of FGT/BIS/FGT at three polarized states as a function of the various stacking orders. (c) Schematic diagrams of two-probe FGT/BIS/FGT MFTJs devices with three different out-plane polar directions using metallic FGT as the electrode. Left and right lead extend to ∓∞. The xy plane is periodic and in a hexagonal lattice for these MFTJs.

a high resistance state. At the P state, the spin-up electrons are majority states in FGT on both sides of BIS at the Fermi level, which dominate the transport with a low resistance state. However, for the spin down, there are two dark blue regions [marked by black rectangles in Fig. 3(a)] with almost no DOS on the left and right FGT regions near the Fermi level,

which means that it is in a high resistance state and may produce an outstanding spin filtering effect. The above analysis can be also directly applied to the AFE-Tail and AFE-Head states.

The difference of TMR in the three ferroelectric polarization states can be understood by the Coulomb potential of

TABLE I. Calculated spin-resolved electron transmission $T_\uparrow$ and $T_\downarrow$, TMR, TER, and spin injection efficiency η at the equilibrium state for FGT/BIS/FGT MFTJs with semi-infinite Fe$_3$GeTe$_2$ electrode for both the left and the right lead.

Configuration and ratio	P state (M↑↑)				AP state (M↑↓)				
	$T_\uparrow$	$T_\downarrow$	$T_{tot} = T_\uparrow + T_\downarrow$	η	$T_\uparrow$	$T_\downarrow$	$T_{tot} = T_\uparrow + T_\downarrow$	η	TMR ($\times 10^6$%)
FE (A)	0.012	5.38×10^{-11}	~0.012	~100%	2.11×10^{-7}	1.02×10^{-7}	3.13×10^{-7}	35%	3.9
AFE-Tail (B)	0.004	8.46×10^{-11}	~0.004	~100%	1.43×10^{-8}	2.48×10^{-8}	3.91×10^{-8}	27%	11.0
AFE-Head (C)	0.025	7.68×10^{-10}	~0.025	~100%	1.18×10^{-7}	2.12×10^{-7}	3.30×10^{-7}	29%	7.6
TER $\dfrac{T_A - T_B}{T_B}$ [a]	182%				701%				
$\dfrac{T_C - T_B}{T_B}$	493%				744%				

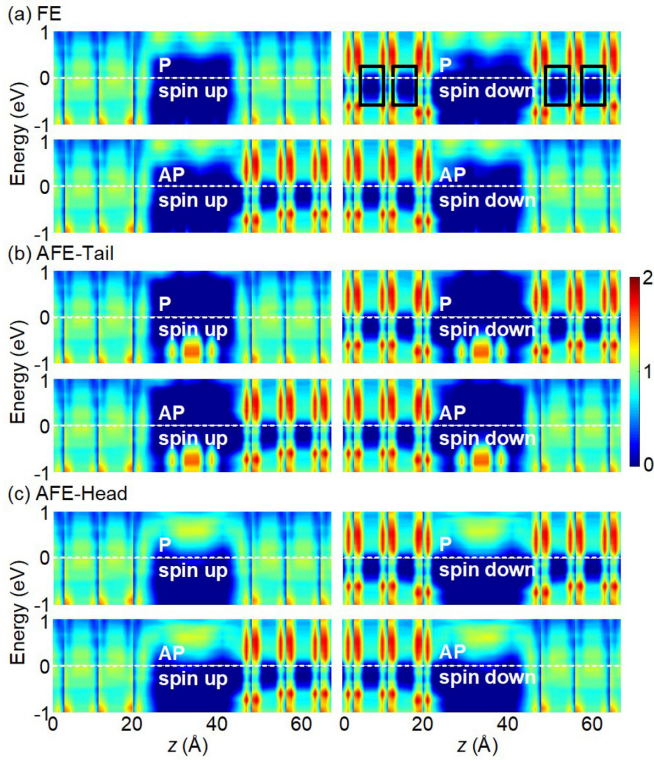[a] T_B is the minimum value for all ferroelectric polarization states.

FIG. 3. Spin-resolved PDOS of the central scattering region along the transport direction (z axis) for FGT/BIS/FGT MFTJs with P and AP magnetization alignments of FGT in the equilibrium state. White dashed lines represent the position of Fermi level. (a) FE state; (b) AFE-Tail state; (c) AFE-Head state.

FIG. 4. The evolution of the Coulomb potential in the central scattering region along the transport direction z axis for the FGT/BIS/FGT MFTJs. (a) FE state; (b) AFE-Tail state; (c) AFE-Head state.

the systems. As illustrated in Fig. 4, one can observe that the potential is symmetric and equal for FGT electrodes on the left and right sides, whereas the potential is smoothly varying at the interface of FGT/BIS. The dipole in the α-In$_2$Se$_3$ forms a built-in electric field denoted by the red dotted lines, and direction of the built-in electric field depends on the dipole polarization. In particular, the potential peak in the center of the α-In$_2$Se$_3$ is different for the three ferroelectric polarization states, i.e., the peak values are 3.63 eV (FE state), 4.68 eV (AFE-Tail), and 2.60 eV (AFE-Head), respectively. The change of potential peak is qualitatively consistent with the distribution of PDOS as shown in Fig. 3, where the length (l) of the low DOS region above the Fermi level (represented by the white dotted line) for the center of the α-In$_2$Se$_3$ bilayer is different, i.e., $l_{AFE-Tail} > l_{FE} > l_{AFE-Head}$. Therefore the reversal of ferroelectric polarization directions of BIS leads to the change of electronic band structures and different transport resistance states in FGT/BIS/FGT MFTJs.

To illustrate the influences of ferroelectric polarization and magnetization alignment on electron transmission in more detail, we calculate the $k_\parallel$-resolved transmission coefficients of the FGT/BIS/FGT MFTJs at the Fermi level in the 2D Brillouin zone as plotted in Fig. 5, which are perpendicular to the transport direction (z axis). In the P state (M $\uparrow\uparrow$), the "hot spots" of the three ferroelectric polarization states of MFTJs are all present around the gamma point of the 2D Brillouin zone and only in the spin-up channel, and the spin down is almost nothing, which means that the perfect
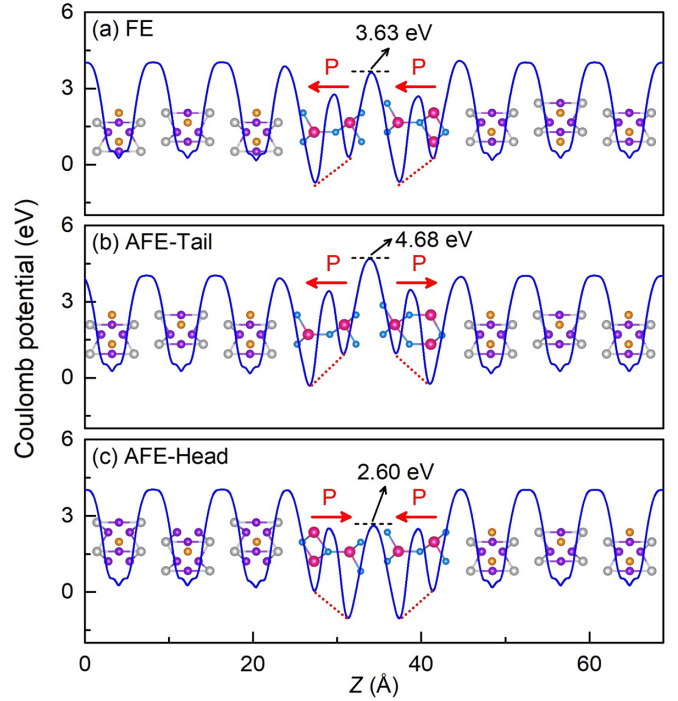
spin filtering effect occurs at the Fermi level. Almost no "hot spots" are observed in the AP state (M $\uparrow\downarrow$) in all polarization states, indicating that the transmission of spin-up and spin-down channels are suppressed in the AP state. Furthermore, it can be clearly observed from Fig. 5 that the transmission
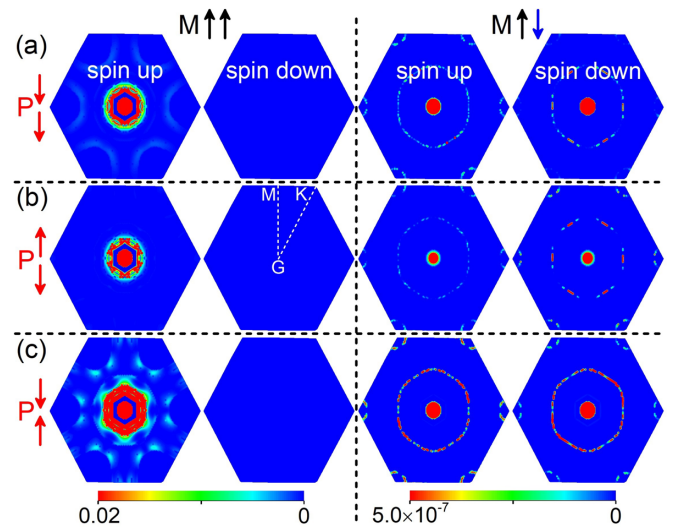

FIG. 5. The $k_\parallel$-resolved transmission coefficients across the FGT/BIS/FGT MFTJs in the 2D Brillouin zone for different ferroelectric polarizations of BIS and P (M $\uparrow\uparrow$) and AP (M $\uparrow\downarrow$) states of FGT at the Fermi level. (a) FE state; (b) AFE-Tail state; (c) AFE-Head state.
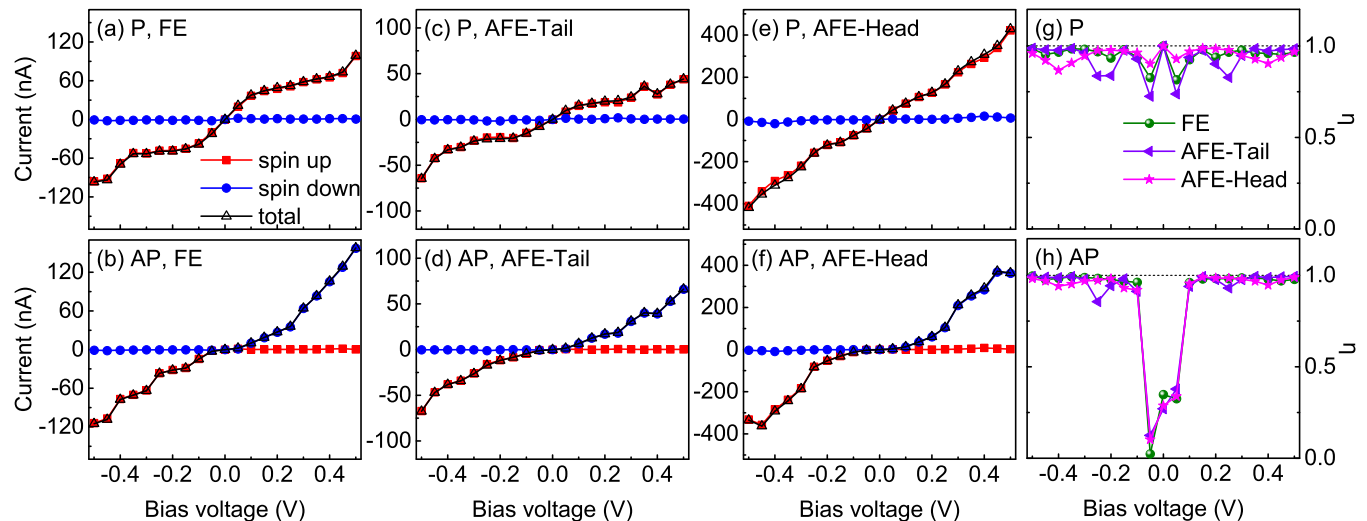
FIG. 6. (a)–(f) The variation of the current and (g)–(h) the spin injection efficiency (η) as a function of the bias voltages for FGT/BIS/FGT MFTJs at three polarized states. (a), (b) FE state; (c), (d) AFE-Tail state; (e), (f) AFE-Head state.

of FGT/BIS/FGT MFTJ is modulated by switching the ferroelectric polarization of BIS. Especially when the polarization of BIS is in the AFE-Tail state, its transmission coefficient is the smallest and significantly lower than the other two polarization states. This is because the BIS interlayer has a high tunneling barrier in the AFE-Tail state due to the reversal of the polarization direction. Therefore the distributions of transmission coefficients in the 2D Brillouin zone further prove the existence of large TMR and TER ratios and a perfect spin filtering effect in these MFTJs in the equilibrium state.

C. Spin-dependent transport properties of MFTJs in the nonequilibrium state

We then study the spin-dependent transport properties of FGT/BIS/FGT vdW MFTJ as a function of bias voltage by calculating I-V curves and spin injection efficiency (η). The bias voltage V_b is set by applying chemical potential on the left (right) electrode as $+V_b/2$ $(-V_b/2)$. Figures 6(a)–6(f) display the corresponding I-V curves of the six combined states. In general, the total current increases monotonically as the bias voltage for all states. For P states as displayed in Figs. 6(a), 6(c) and 6(e), the systems exhibit a nearly perfect spin filtering effect, where only spin-up electrons are allowed to transit through the barrier mainly due to the P arrangement of magnetic order. Interestingly, for AP states as demonstrated in Figs. 6(b), 6(d) and 6(f), the systems exhibit a bias voltage-dependent spin filtering effect, i.e., only the spin-up (spin-down) current is allowed for negative (positive) voltage. Therefore the MFTJs can also be used as spin valves that the spin channel can be flexibly manipulated. Moreover, as shown in Fig. 6(g), the spin injection efficiency (η) of these MFTJs for P state approaches 100% at zero bias voltage and oscillates with bias voltages. For the AP state, η is less than 40% at a low bias range of (-0.05, 0.05 V), but it approaches 100% at other bias ranges. The above results indicate that these MFTJs can achieve a significant spin filtering effect in a wide range of bias voltage, which is expected to be applied in spintronic devices.

To understand the interesting spin filtering effect described above, we calculate the electron transmission coefficients varying with energy at different bias voltages (± 0.4, ± 0.2, and 0.0 V) in Fig. 7. According to Eq. (1), the integral of the electron transmission coefficients in the bias voltage window equals the current, implying that the area enclosed by the transmission spectrum and the energy axis in the bias voltage window can roughly reflect the current. At the P state, for these MFTJs in FE and AFE-Tail states [see Figs. 7(a) and 7(b)], there is an almost only spin-up transmission spectrum in all bias windows, corresponding to an almost perfect spin filtering effect. For the AFE-Head state [see Fig. 7(c)], the spin-down transmission spectrum obviously appears at ± 0.4 V, so its η is significantly smaller than the MFTJs in the other two polarization states, which is consistent with our calculation results of η. At the AP state, when the bias voltage is positive(negative), the electron transmission spectrums of all MFTJs almost only show in the spin-down(spin-up) channel in the corresponding windows, which further verifies the phenomenon that the different spin channel is prohibited under the opposite bias voltage. Moreover, the transmission coefficient at Fermi level under the 0.0 V only appears in the spin-up channel, and there is almost no value in the AP state, which not only indicates the perfect spin filtering effect in P state but also implies the emergence of a large TMR ratio in these MFTJs.

D. The influence of electrodes

Previous studies have demonstrated that electrode structure is important to device performance [15,57]. In this section, we study the influence of symmetric (Cu-MFTJ-Cu) and asymmetric (Cu-MFTJ-FGT) electrodes on the performance of FGT/BIS/FGT MFTJs. Before building the device model, we first need to determine the detailed contact geometry between the Cu electrode and the central scattering region. As shown in Figs. 8(a) and 8(b), in the Cu-FGT heterostructure, the $\sqrt{3} \times \sqrt{3}$ Cu(111) slab is matched with the 1×1 monolayer FGT. Since the Cu(111) slab is composed of three
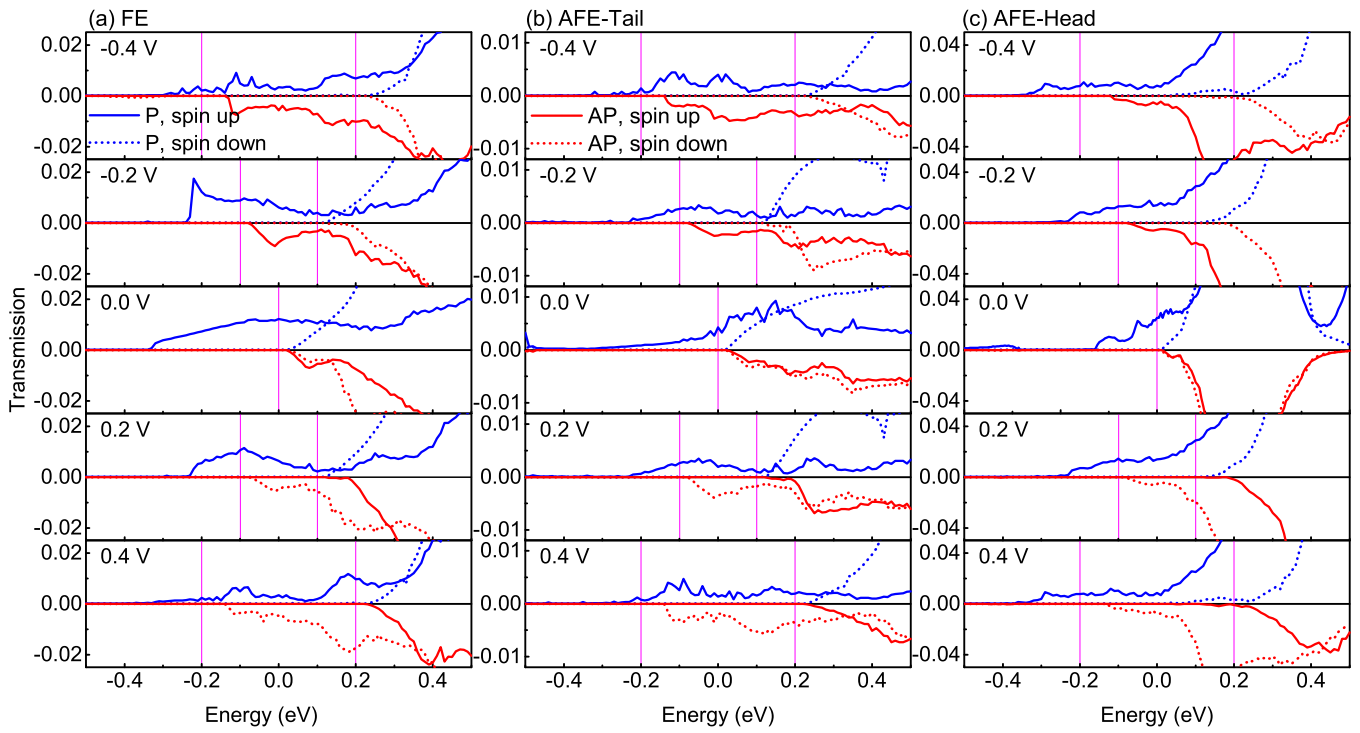
FIG. 7. Transmission coefficients as a function of energy at different bias voltages (±0.4, ±0.2, and 0.0 V) for FGT/BIS/FGT MFTJs. The magenta vertical lines represent the bias voltage window used to calculate the current. The Fermi energy is set to 0 eV. (a) FE state; (b) AFE-Tail state. (c) AFE-Head state; 0 V means that the devices are in equilibrium states. Note that the negative transmission values here represent at AP state.
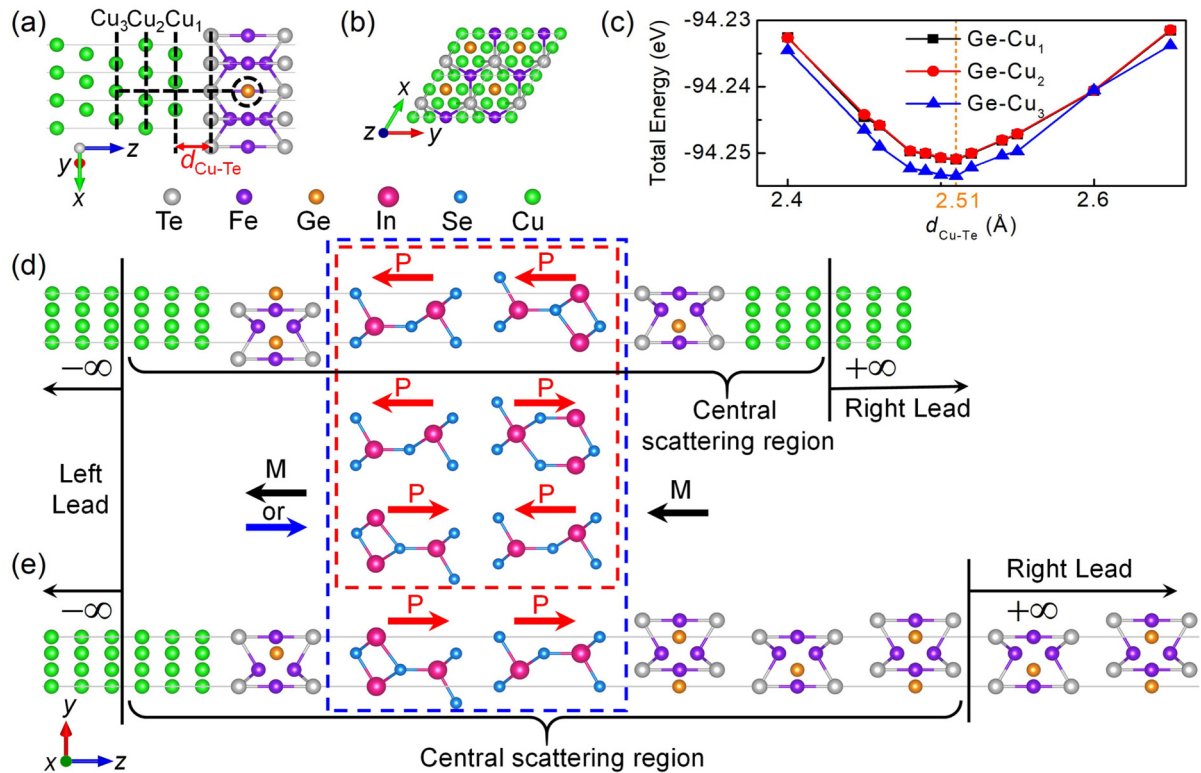

FIG. 8. (a) Side view and (b) top view of the crystal structure of the Cu/FGT heterostructure constructed by monolayer FGT and Cu(111) slab. (c) The total energy of Cu/FGT heterostructure with three stacking orders vs the various interlayer distance d_{Cu-Te}. The schematic diagram of the same electrode Cu (d) and different electrodes Cu/FGT (e) used on the left and right sides of the FGT/BIS/FGT MFTJs.

TABLE II. Calculated spin-resolved electron transmission $T_\uparrow$ and $T_\downarrow$, TMR, TER, and spin injection efficiency η at the equilibrium state for FGT/BIS/FGT MFTJs with symmetrical Cu/Cu leads and asymmetric Cu/FGT leads on the left and right sides of the central scattering region.

L/R lead	Configuration and ratio	P state (M↑↑)				AP state (M↑↓)				TMR ($\times 10^3$%)
		$T_\uparrow$	$T_\downarrow$	$T_{tot} = T_\uparrow + T_\downarrow$	η	$T_\uparrow$	$T_\downarrow$	$T_{tot} = T_\uparrow + T_\downarrow$	η	
Cu/Cu	FE (A)	1.74×10^{-4}	1.62×10^{-6}	1.76×10^{-4}	98%	2.68×10^{-6}	4.93×10^{-6}	7.61×10^{-6}	29%	2.2
	AFE-Tail (B)	5.18×10^{-5}	6.08×10^{-7}	5.24×10^{-5}	98%	2.47×10^{-6}	9.65×10^{-7}	3.43×10^{-6}	44%	1.4
	AFE-Head (C)	1.02×10^{-3}	1.05×10^{-5}	1.03×10^{-3}	98%	1.92×10^{-5}	1.73×10^{-5}	3.65×10^{-5}	5%	2.7
	TER $\dfrac{T_A - T_B}{T_B}$	235%				122%				
	$\dfrac{T_C - T_B}{T_B}$	1868%				964%				
Cu/FGT	FE-Down (A)[a]	1.15×10^{-4}	2.58×10^{-8}	$\sim 1.15 \times 10^{-4}$	$\sim$100%	3.60×10^{-6}	2.18×10^{-8}	3.62×10^{-6}	99%	3.1
	AFE-Tail (B)	1.74×10^{-5}	1.61×10^{-9}	$\sim 1.74 \times 10^{-5}$	$\sim$100%	1.29×10^{-6}	6.04×10^{-9}	1.30×10^{-6}	99%	1.2
	AFE-Head (C)	3.16×10^{-4}	3.70×10^{-8}	$\sim 3.16 \times 10^{-4}$	$\sim$100%	1.13×10^{-5}	7.50×10^{-8}	1.14×10^{-5}	99%	2.7
	FE-Up (D)	1.29×10^{-4}	1.26×10^{-7}	$\sim 1.29 \times 10^{-4}$	$\sim$100%	1.61×10^{-6}	9.35×10^{-9}	1.62×10^{-6}	99%	7.9
	$\dfrac{T_A - T_B}{T_B}$	561%				179%				
	$\dfrac{T_C - T_B}{T_B}$	1719%				775%				
	TER $\dfrac{T_D - T_B}{T_B}$	645%				25%				
	$\dfrac{T_D - T_A}{T_A}$ [b]	13%				124%				

[a]Due to the asymmetric electrodes, the two arrangements of the bilayer In_2Se_3 in the FE state in which the ferroelectric polarization directions are both up and down are different.

[b]FE-Down and FE-Up are two completely opposite ferroelectric polarization states produced by asymmetric electrodes. They can switch flexibly by a uniform electric field and show different electroresistance states, which is a typical ferroelectric TJ.

Cu atomic layers (labeled $Cu_{1/2/3}$) in a repetitive period [see Fig. 8(a)], the Cu-FGT heterostructure can form three stacking orders (Ge-$Cu_{1/2/3}$), where Ge-$Cu_{1/2/3}$ represents the Ge atom (marked by a dotted circle) that stacks vertically on top of the Cu atom. As depicted in Fig. 8(c), the optimal distances d_{Cu-Te} between FGT monolayer and Cu(111) slab for the three stacking configurations are determined by calculating the total energy as a function of d_{Cu-Te}. We can find that the optimal stacking order is Ge-Cu_3, and the interlayer distance d_{Cu-Te} is 2.51 Å. Based on the geometries in the aforementioned section, we construct two additional MFTJs (Cu-FGT/BIS/FGT-Cu and Cu-FGT/BIS/FGT MFTJs) devices with different electrodes as shown in Figs. 8(d) and 8(e). The symmetric Cu-FGT/BIS/FGT-Cu MFTJ has three ferroelectric polarization states as shown in the red dotted rectangle [see Fig. 8(d)], while the asymmetric Cu-FGT/BIS/FGT MFTJ harbors four ferroelectric polarization states [see the blue dotted rectangle in Fig. 8(e)]. For the above two MFTJs, the monolayer FGT near the Cu electrode is taken as the ferromagnetic free layer.

In Table II, we summarize the transport results at the Fermi energy. Among the three ferroelectric polarization states, the AFE-Tail state displays minimum transmission coefficients in the two MFTJs, which is consistent with the result in Table I. For the Cu-FGT/BIS/FGT-Cu MFTJ, the η is up to 98% at the P state, and the maximum TMR (TER) ratio is 2700% (1868%). For Cu-FGT/BIS/FGT MFTJ, the perfect spin

filtering effect can be achieved in both the P and the AP states, and the maximum TMR and TER ratios are 7900 and 1719%, respectively. It is worth mentioning because of the asymmetric electrode in Cu-FGT/BIS/FGT MFTJ, the FE-Up state and FE-Down of BIS are two completely opposite ferroelectric polarization arrangements and these two polarization states can be easily switched with each other by applying a unified electric field in the experiment. In particular, the TER ratios obtained by switching directions between the two ferroelectric polarization states (FE-Up and FE-Down) are 13 and 124% in the P and AP states, respectively. The above results indicate that the inclusion of symmetric Cu/Cu and asymmetric Cu/FGT electrodes in MFTJs can significantly increase the TER ratio and preserve large η, whereas TMR is still considerable.

IV. SUMMARY

In summary, we systemically investigate the spin-resolved electronic transport properties of the FGT/BIS/FGT vdW MFTJs by first-principles calculations. We demonstrate multiple nonvolatile resistance states in the MFTJs and the possibility to manipulate these states. The maximum TMR ratio is 1.1×10^7%, and a 1868% TER ratio can be obtained by changing the electrodes. In addition, a perfect spin filtering effect is observed and the spin channel can be flexibly controlled. Our work provides an ideal platform to design multifunctional vdW MFTJs for spintronic applications.

Experimentally, the polarization direction of ferroelectric materials can be tuned by an electric field. Our results and previous studies [39,58] demonstrate that the ferroelectric ground state of BIS is the AFE-Tail. So there are two polarization switching combinations for our FGT/BIS/FGT MFTJ, i.e., the AFE-Tail→FE and the AFE-Tail→AFE-Head. First, for the AFE-Tail→FE case, by applying a uniform out-of-plane electric field, the opposite aligned polarization directions of the BIS can be reversed to coincide with the direction of the electric field. Previous experiments have demonstrated that the electric field can flip the polarization direction of In_2Se_3 [25,59,60]. In addition, the intercorrelated polarization switching mechanism of in-plane and out-of-plane ferroelectricity of α-In_2Se_3 nanoflakes has also been experimentally observed [35]. Therefore applying an in-plane electric field is a feasible strategy to experimentally realize the AFE-Tail→AFE-head state for BIS.

Note that Su *et al.* reported that $Fe_mGeTe_2/In_2Se_3/Fe_nGeTe_2$ (m, n = 3, 4, 5; m ≠ n) MFTJs exhibit multiple nonvolatile resistance states [30], which is different from our work in two aspects. First, the device structures are different, i.e., we use bilayer In_2Se_3 as a barrier layer and FGT as an electrode, whereas Su *et al.* [30] used monolayer In_2Se_3 as a barrier layer and $PtTe_2$ as an electrode. Because the MFTJ requires an asymmetric structure on both sides of the ferroelectric layer, in Su *et al.* [30] $Fe_{m/n}GeTe_2$ (m ≠ n) was only used as a ferromagnetic layer. Differently, the FGT in our MFTJs not only acts as a ferromagnetic layer but also serves as an electrode due to the intrinsic asymmetry of the BIS introduced by different polarization states. As a result, our MFTJs have fewer material interfaces and are easier to fabricate experimentally. Second, our MFTJs demonstrate more nonvolatile resistance states, i.e., six states under symmetric FGT electrodes and eight under asymmetric Fe_3GeTe_2/Cu electrodes and better performance than the previous study.

APPENDIX A: THE BINDING ENERGY OF FGT/In_2Se_3 INTERFACE

To verify the stability of the vdW interface in In_2Se_3-based MFTJs, we calculated the binding energy (E_B) of FGT/In_2Se_3 interface with different stacking orders, which is
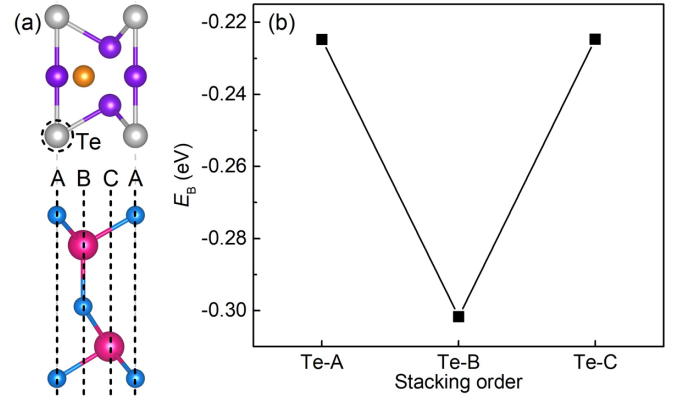

FIG. 9. The side view of the crystal structure of the FGT/In_2Se_3 heterostructure. (b) The binding energy as a function of different stacking orders of FGT/In_2Se_3 heterostructure.

defined as

$$E_B = E_{FGT/In_2Se_3} - E_{FGT} - E_{In_2Se_3}, \tag{A1}$$

where E_{FGT/In_2Se_3} and $E_{FGT}(E_{In_2Se_3})$ are the total energies of the FGT/In_2Se_3 heterostructure and isolated FGT(In_2Se_3) monolayer, respectively. The obtained E_B are all negative and robust against variation of stacking orders [see Fig. 9], indicating that the interfaces of MFTJs linked by vdW forces are stable.

APPENDIX B: THE MAGNETIC ANISOTROPY ENERGY OF FGT/BIS/FGT HETEROSTRUCTURE

To clarify the magnetic easy axis of FGT under the proximity effect of BIS, we calculated the magnetic anisotropy energy (MAE) of FGT/BIS/FGT heterojunction. The MAE is defined as MAE $= E_\perp - E_\parallel$, where $E_\perp$ and $E_\parallel$ denote the total energies for FGT magnetization in out-of-plane and in-plane directions, respectively. As shown in Fig. 10, the calculated MAE is negative for all polarization states of BIS,
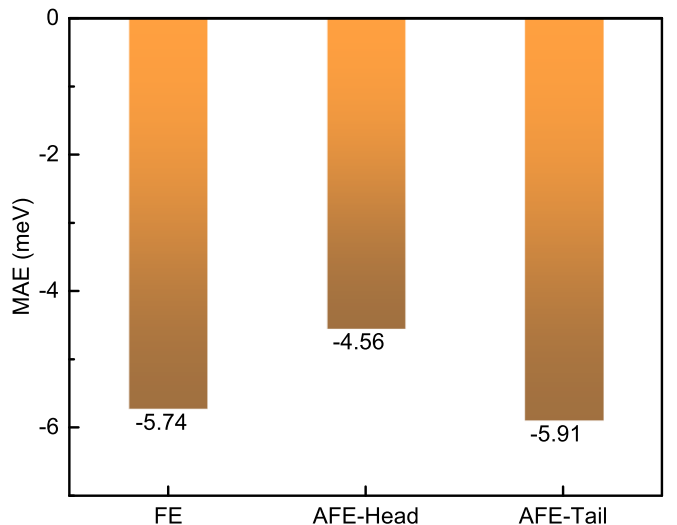

FIG. 10. The MAE of the FGT/BIS/FGT heterostructure [see Fig. 2(a)] as a function of different polarization states.
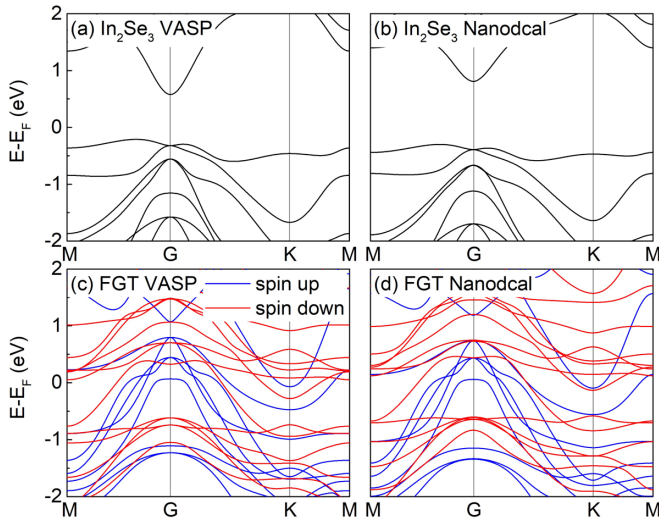
FIG. 11. (a)–(d) The band structures of monolayer In_2Se_3 and FGT, (a) and (c) by using VASP package, (b) and (d) by using Nanodcal package.

FIG. 12. The (a) TMR, (b) TER, and (c), (d) spin injection efficiency η of FGT/BIS/FGT MFTJ in different polarization states as functions of in-plane biaxial strain.

indicating that the ferroelectricity of BIS does not affect the magnetic easy axis of FGT and the out-of-plane easy axis is still preserved.

APPENDIX C: THE BAND STRUCTURES OF MONOLAYER In_2Se_3 AND FGT

To ensure the consistency of the calculation results between the two softwares, we used the VASP and Nanodcal packages to calculate the electronic band structures of monolayer In_2Se_3 and FGT. The corresponding results are shown in Fig. 11. One can find that the band structures obtained from the two software are basically consistent, especially for the bands near the Fermi level, which shows the credibility of the electron transport properties performed by the Nanodcal package.
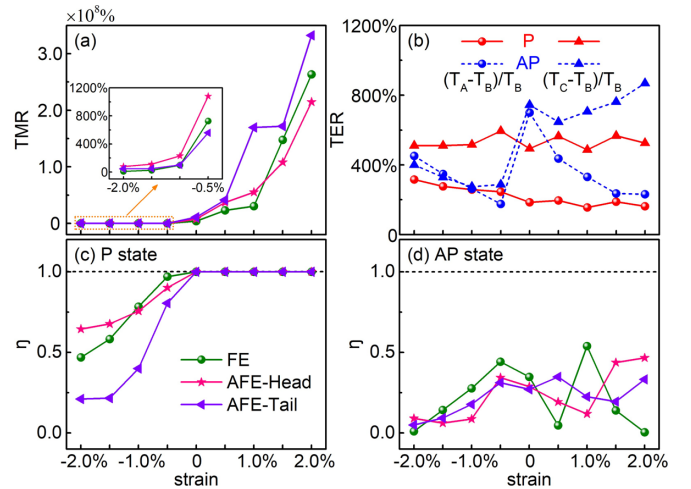
APPENDIX D: THE EFFECT OF STRAIN

The lattice mismatch between FGT and α-In_2Se_3 is about 1.0%. To clarify the effect of strain on the transport properties of the MFTJ, we calculated TMR, TER, and η as a function of in-plane biaxial strain for FGT/BIS/FGT MFTJ as shown in Fig. 12. We can find that (i) as displayed in Fig. 12(a), for all three polarization states under tensile strain, the TMR increases with increasing stress, whereas the TMR decreases under compressive strain; (ii) as shown in Fig. 12(b), for the P state, TER remains stable in the strain range; for the AP state, the TER obtained by switching the ferroelectric polarization direction of BIS between AFE-Tail and FE states gradually increases after the strain is greater than $\pm 0.5\%$, whereas the TER from switching between AFE-Tail and AFE-Head states decreases with the increase of tensile stress; (iii) as shown in Fig. 12(c), for all three polarization states in the P state, η decreases with increasing compressive stress, whereas it is robust and maintains perfect spin filtering effect under tensile stress; (iv) for the AP state as displayed in Fig. 12(d), η oscillates with strain. Therefore the above results suggest that strain is an effective approach to modulate the transport properties of MFTJs.

[1] A. Brataas, A. D. Kent, and H. Ohno, Nat. Mater. **11**, 372 (2012).

[2] C. Chappert, A. Fert, and F. N. V. Dau, Nat. Mater. **6**, 813 (2007).

[3] J.-G. J. Zhu and C. Park, Mater. Today **9**, 36 (2006).

[4] M. Julliere, Phys. Lett. A **54**, 225 (1975).

[5] H. Kohlstedt, N. A. Pertsev, J. Rodriguez Contreras, and R. Waser, Phys. Rev. B **72**, 125341 (2005).

[6] C.-G. Duan, S. S. Jaswal, and E. Y. Tsymbal, Phys. Rev. Lett. **97**, 047201 (2006).

[7] M. Gajek, M. Bibes, S. Fusil, K. Bouzehouane, J. Fontcuberta, A. Barthélémy, and A. Fert, Nat. Mater. **6**, 296 (2007).

[8] M. Y. Zhuravlev, S. Maekawa, and E. Y. Tsymbal, Phys. Rev. B **81**, 104419 (2010).

[9] E. Y. Tsymbal, Science **313**, 181 (2006).

[10] J. P. Velev, C.-G. Duan, J. D. Burton, A. Smogunov, M. K. Niranjan, E. Tosatti, S. S. Jaswal, and E. Y. Tsymbal, Nano Lett. **9**, 427 (2009).

[11] D. Pantel, S. Goetze, D. Hesse, and M. Alexe, Nat. Mater. **11**, 289 (2012).

[12] V. Garcia, M. Bibes, L. Bocher, S. Valencia, F. Kronast, A. Crassous, X. Moya, S. Enouz-Vedrenne, A. Gloter, D. Imhoff, C. Deranlot, N. D. Mathur, S. Fusil, K. Bouzehouane, and A. Barthelemy, Science **327**, 1106 (2010).

[13] V. S. Borisov, S. Ostanin, S. Achilles, J. Henk, and I. Mertig, Phys. Rev. B **92**, 075137 (2015).

[14] T. R. Paudeland E. Y. Tsymbal, ACS Appl. Mater. Interfaces **11**, 15781 (2019).

[15] L. Pan, L. Huang, M. Zhong, X.-W. Jiang, H.-X. Deng, J. Li, J.-B. Xia, and Z. Wei, Nanoscale **10**, 22196 (2018).

[16] X. Li, J.-T. Lü, J. Zhang, L. You, Y. Su, and E. Y. Tsymbal, Nano Lett. **19**, 5133 (2019).

[17] Z. Yan, R. Zhang, X. Dong, S. Qi, and X. Xu, Phys. Chem. Chem. Phys. **22**, 14773 (2020).

[18] L. Zhang, T. Li, J. Li, Y. Jiang, J. Yuan, and H. Li, J. Phys. Chem. C **124**, 27429 (2020).

[19] Z. Yan, X. Jia, X. Shi, X. Dong, and X. Xu, Appl. Phys. Lett. **118**, 223503 (2021).

[20] Y. Feng, X. Wu, L. Hu, and G. Gao, J. Mater. Chem. C **8**, 14353 (2020).

[21] Y. Feng, X. Wu, and G. Gao, Appl. Phys. Lett. **116**, 022402 (2020).

[22] Y. Zhu, X. Y. Guo, L. N. Jiang, Z. R. Yan, Y. Yan, and X. F. Han, Phys. Rev. B **103**, 134437 (2021).

[23] L. Kang, P. Jiang, H. Hao, Y. Zhou, X. Zheng, L. Zhang, and Z. Zeng, Phys. Rev. B **101**, 014105 (2020).

[24] L. Kang, P. Jiang, H. Hao, Y. Zhou, X. Zheng, L. Zhang, and Z. Zeng, Phys. Rev. B **103**, 125414 (2021).

[25] S. Wan, Y. Li, W. Li, X. Mao, W. Zhu, and H. Zeng, Nanoscale **10**, 14885 (2018).

[26] X. Wang, C. Zhu, Y. Deng, R. Duan, J. Chen, Q. Zeng, J. Zhou, Q. Fu, L. You, S. Liu, J. H. Edgar, P. Yu, and Z. Liu, Nat. Commun. **12**, 1109 (2021).

[27] X. Li, Y. Su, M. Zhu, F. Zheng, P. Zhang, J. Zhang, and J.-T. Lü, Phys. Rev. Appl. **16**, 034052 (2021).

[28] L. Kang, P. Jiang, N. Cao, H. Hao, X. Zheng, L. Zhang, and Z. Zeng, Nanoscale **11**, 16837 (2019).

[29] L. Zhang, Y. Yang, J. Chen, X. Zheng, L. Zhang, L. Xiao, and S. Jia, Phys. Chem. Chem. Phys. **22**, 18548 (2020).

[30] Y. Su, X. Li, M. Zhu, J. Zhang, L. You, and E. Y. Tsymbal, Nano Lett. **21**, 175 (2020).

[31] B. Chen, J. Yang, H. Wang, M. Imai, H. Ohta, C. Michioka, K. Yoshimura, and M. Fang, J. Phys. Soc. Jpn. **82**, 124711 (2013).

[32] Q. Li, M. Yang, C. Gong, R. V. Chopdekar, A. T. N'Diaye, J. Turner, G. Chen, A. Scholl, P. Shafer, E. Arenholz, A. K. Schmid, S. Wang, K. Liu, N. Gao, A. S. Admasu, S.-W. Cheong, C. Hwang, J. Li, F. Wang, X. Zhang *et al.*, Nano Lett. **18**, 5974 (2018).

[33] Y. Deng, Y. Yu, Y. Song, J. Zhang, N. Z. Wang, Z. Sun, Y. Yi, Y. Z. Wu, S. Wu, J. Zhu, J. Wang, X. H. Chen, and Y. Zhang, Nature (London) **563**, 94 (2018).

[34] W. Ding, J. Zhu, Z. Wang, Y. Gao, D. Xiao, Y. Gu, Z. Zhang, and W. Zhu, Nat. Commun. **8**, 14956 (2017).

[35] B. Lv, Z. Yan, W. Xue, R. Yang, J. Li, W. Ci, R. Pang, P. Zhou, G. Liu, Z. Liu, W. Zhu, and X. Xu, Mater. Horiz. **8**, 1472 (2021).

[36] Y. Zhou, D. Wu, Y. Zhu, Y. Cho, Q. He, X. Yang, K. Herrera, Z. Chu, Y. Han, M. C. Downer, H. Peng, and K. Lai, Nano Lett. **17**, 5508 (2017).

[37] A. Belianinov, Q. He, A. Dziaugys, P. Maksymovych, E. Eliseev, A. Borisevich, A. Morozovska, J. Banys, Y. Vysochanskii, and S. V. Kalinin, Nano Lett. **15**, 3808 (2015).

[38] K. Yasuda, X. Wang, K. Watanabe, T. Taniguchi, and P. Jarillo-Herrero, Science **372**, 1458 (2021).

[39] J. Ding, D.-F. Shao, M. Li, L.-W. Wen, and E. Y. Tsymbal, Phys. Rev. Lett. **126**, 057601 (2021).

[40] P. E. Blöchl, Phys. Rev. B **50**, 17953 (1994).

[41] G. Kresse and J. Furthmüller, Phys. Rev. B **54**, 11169 (1996).

[42] J. P. Perdew, J. A. Chevary, S. H. Vosko, K. A. Jackson, M. R. Pederson, D. J. Singh, and C. Fiolhais, Phys. Rev. B **46**, 6671 (1992).

[43] E. R. Johnsonand A. D. Becke, J. Chem. Phys. **123**, 024101 (2005).

[44] J. Taylor, H. Guo, and J. Wang, Phys. Rev. B **63**, 245407 (2001).

[45] J. Taylor, H. Guo, and J. Wang, Phys. Rev. B **63**, 121104(R) (2001).

[46] J. M. Soler, E. Artacho, J. D. Gale, A. García, J. Junquera, P. Ordejón, and D. Sánchez-Portal, J. Phys.: Condens. Matter **14**, 2745 (2002).

[47] Y. Meirand N. S. Wingreen, Phys. Rev. Lett. **68**, 2512 (1992).

[48] S. Datta, *Electronic Transport in Mesoscopic Systems* (Cambridge University Press, 1995).

[49] S. Yuasa, T. Nagahama, A. Fukushima, Y. Suzuki, and K. Ando, Nat. Mater. **3**, 868 (2004).

[50] L. L. Taoand J. Wang, Appl. Phys. Lett. **108**, 062903 (2016).

[51] J. Xiao, H. Zhu, Y. Wang, W. Feng, Y. Hu, A. Dasgupta, Y. Han, Y. Wang, D. A. Muller, L. W. Martin, P. Hu, and X. Zhang, Phys. Rev. Lett. **120**, 227601 (2018).

[52] R. B. Jacobs-Gedrim, M. Shanmugam, N. Jain, C. A. Durcan, M. T. Murphy, T. M. Murray, R. J. Matyi, R. L. Moore, and B. Yu, ACS Nano **8**, 514 (2013).

[53] X. Taoand Y. Gu, Nano Lett. **13**, 3501 (2013).

[54] Y. Yang, L. Zhang, J. Chen, X. Zheng, L. Zhang, L. Xiao, and S. Jia, Nanoscale **13**, 8555 (2021).

[55] H.-J. Deiseroth, K. Aleksandrov, C. Reiner, L. Kienle, and R. K. Kremer, Eur. J. Inorg. Chem. **2006**, 1561 (2006).

[56] S. Popović, A. Tonejc, B. Gržeta-Plenković, B. Čelustka, and R. Trojko, J. Appl. Crystallogr. **12**, 416 (1979).

[57] W. Rotjanapittayakul, W. Pijitrojana, T. Archer, S. Sanvito, and J. Prasongkit, Sci. Rep. **8**, 4779 (2018).

[58] J. Ding, L. Wen, W. Chai, S. Liu, R. Li, H. Li, and Y. Zhang, Appl. Surf. Sci. **567**, 150871 (2021).

[59] S. Wang, L. Liu, L. Gan, H. Chen, X. Hou, Y. Ding, S. Ma, D. W. Zhang, and P. Zhou, Nat. Commun. **12**, 53 (2021).

[60] F. Xue, X. He, J. R. D. Retamal, A. Han, J. Zhang, Z. Liu, J.-K. Huang, W. Hu, V. Tung, J.-H. He, L.-J. Li, and X. Zhang, Adv. Mater. **31**, 1901300 (2019).